peakTree: A framework for structure-preserving radar Doppler spectra analysis

Martin Radenz[1], Johannes Bühl[1], Patric Seifert[1], Hannes Griesche[1], and Ronny Engelmann[1]

[1]Leibniz Institute for Tropospheric Research (TROPOS), Leipzig, Germany

Correspondence: Martin Radenz (radenz@tropos.de)

Abstract. Clouds are frequently composed of more than one particle population even at smallest scales. Cloud radar observations contain information on multiple particle species, when there are distinct peaks in the Doppler spectrum. Complex multi-peaked situations are not captured by established algorithms. In this study we propose a new algorithm, that recursively represents the subpeaks as nodes in a binary tree. Using this tree data structure to represent the peaks of a Doppler spectrum it is possible to drop all a-priori assumptions on the number and arrangement of subpeaks. The approach is rigid, unambiguous and can provide a basis for advanced analysis methods. The applicability is briefly demonstrated in a case study, where the tree structure was used to separate two particle populations in an Arctic multi-layered mixed-phase cloud, which was observed during the research vessel Polarstern expedition PS106.

1 Introduction

The characterization of mixed-phase clouds and associated microphysical processes poses a challenge to experimentalists, therefore these processes are still not well represented in general circulation models (Fan et al., 2011). In-situ instruments are subject to icing under the presence of supercooled liquid water, and the wide range of possible hydrometeor types require the deployment of instruments of which each can only cover a certain aspect of the whole hydrometeor distribution (Baumgardner et al., 2017; Korolev et al., 2017).

Frequently, cloud radars are used for the investigation of mixed-phase clouds (Bühl et al., 2017). At Ka- and W-band, cloud radars are sensitive to scattering from the whole range of possible hydrometeors, ranging from cloud droplets to graupel (e.g. Kollias et al., 2007a; Fukao and Hamazu, 2014). In general cloud radars are Doppler-capable and provide the backscattered signal as a function of Doppler velocity, commonly called Doppler spectrum (Wakasugi et al., 1986). When multiple particle populations are present in the observed volume, they are frequently represented as distinct peaks in the Doppler spectrum. (e.g. Shupe et al., 2004; Luke et al., 2010; Verlinde et al., 2013; Yu et al., 2014; Kalesse et al., 2016; Kollias et al., 2016). The properties of a multi-peak situation can only partly be represented by the moments of a single peak algorithm, which causes errors in the target classification and subsequent microphysical retrievals. A multitude of approaches are available to classify clouds and retrieve water contents, particle sizes and number concentrations (for example Clothiaux et al. 2000; Wang and Sassen 2002; Wang et al. 2004; Hogan et al. 2006; Illingworth et al. 2007; an overview is provided in Shupe et al.

2016 and Zhao et al. 2012). Almost all established algorithms are based on the assumption of mono-modal hydrometeor size distributions, which likely causes significant errors in multi-peaked situations.

When multi-peak situations are investigated, commonly strong assumptions are made on the structure of the Doppler spectrum, e.g. only one liquid and one ice peak (Shupe et al., 2004) or liquid, newly formed ice and ice from above (Rambukkange
5 et al., 2011). Relationships between subpeaks in neighboring Doppler spectra have to be interpreted manually. In more recent work, sophisticated methods were introduced to identify the liquid peak in a multipeak situation (Luke et al., 2010; Yu et al., 2014) or to separate the liquid peak from drizzle (Luke and Kollias, 2013). In a further step Oue et al. (2018), using the microARSCL algorithm (Kollias et al., 2007b; Luke et al., 2008), allow a primary peak to be split into two subpeaks, but the left peak (faster falling) is assumed to have a higher reflectivity. Additionally, a noise-floor separated secondary peak is
10 possible. In summary, prior approached either used just a list of peaks (sorted by reflectivity or mean velocity) or a predefined structure based on strong assumptions on peak arrangement. Such strong constraints may be justified for short periods at single geographic locations, but are not suitable for a general approach. Up to now, no generic and flexible formalism is available, to describe an arbitrary number of subpeaks of a Doppler spectrum without a-priori assumption on the structure.

In this study it will be shown how a binary tree representation of multiple peaks can provide a rigid, hence flexible formalism
15 to represent the peaks in a Doppler spectrum. The tree structure allows an arbitrary number of subpeaks in any arrangement, while at the same time being unambiguous and easily accessible by algorithms. The software implementing the algorithm easily applicable to other radar systems and available openly. The study is structured as follows: The dataset used for demonstration of the tree generating peak-separation technique is introduced in Section 2. In Section 3, the peak separation algorithm is presented. Section 4 is dedicated to the presentation of a case study in which the algorithm was used to separate particle
20 populations in an Arctic mixed-phase cloud. Discussions and conclusions are covered in Section 5.

2 Dataset

During the Physical feedbacks of Arctic planetary boundary level Sea ice, Cloud and AerosoL (PASCAL) campaign (PS106; Wendisch et al., in press) a cloud radar Mira-35 was operated as part of the OCEANET suite on R/V Polarstern (Griesche et al., in preparation) together with, amongst other instruments, a Polly^{XT} Raman and polarization lidar (Engelmann et al.,
25 2016) and a HATPRO 14-channel microwave radiometer (Rose et al., 2005). Mira-35 is a magnetron-based pulsed 35-GHz cloud radar with polarisation and Doppler capabilities (Görsdorf et al., 2015). During the campaign, Mira-35 was operated in linear-depolarization-ratio (LDR) mode. The pulse repetition frequency was $5\,\mathrm{kHz}$ and one Doppler spectrum was based on the fast Fourier transform of 256 pulses, yielding a Doppler resolution of $0.082\,\mathrm{m\,s^{-1}}$. The radar was operated in vertical-stare mode. It was based on a leveling platform which actively corrected for pitch and roll movement of the ship. Vertical movement
30 of the radar was corrected at a rate of $4\,\mathrm{Hz}$ using the ship motion data originally recorded at $20\,\mathrm{Hz}$. For the datasets of Arctic clouds presented in here, the active stabilization was not available anymore due to a hardware failure. In the scope of this study, therefore the Doppler spectra acquired within $10\,\mathrm{s}$ were averaged incoherently to suppress the ship pitch and roll motion, while the vertical motion was still corrected at a rate of $4\,\mathrm{Hz}$. The lack of active pitch and roll suppression lead to an accuracy of the

zenith pointing of $1.5°$. For horizontal wind velocities below $10\,\mathrm{m\,s^{-1}}$, the bias introduced to the observed vertical velocity thus is below $0.2\,\mathrm{m\,s^{-1}}$.

By default, Mira-35 provides noise-cleaned compressed Doppler spectra (zspc) and moment data separately for meteorological targets and atmospheric plankton (Görsdorf et al., 2015). Further data analysis is subject to the operator of the cloud

5 radar, to which the zspc data provides a solid base for potential application of peak separation techniques. Accurate measurements of polarization variables, like the LDR, depend strongly on instrument hardware due to polarization leakage. This is especially true for spectral estimates of the LDR. The lowest LDR observable (integrated cross-polarization ratio ICPR) with this version of Mira-35 was estimated in the presence of light drizzle with the approach of Myagkov et al. (2015) and found to be $-27.6\,\mathrm{dB}$. A second effect that has to be considered while calculating the LDR, is the noise level in the cross channel.

10 If the signal in the cross channel is below the noise level, the LDR is determined solely by the signal in the co channel and no meaningful information on the polarization state of the received signal can be derived (Matrosov and Kropfli, 1993). Hence, when calculating the LDR (Eq. A5) only bins with signal above the noise level in the cross-channel are taken into account.

3 Algorithm

3.1 Transforming the Doppler spectrum into the tree representation

15 The algorithm explained in here transforms each Doppler spectrum with its (sub-)peaks into a full binary tree structure. A full binary tree is a directed graph with one root node and recursively each node might possess either two child nodes or none (Garnier and Taylor, 2009). Here, a node is related to a part of the Doppler spectrum that contains at least one peak. Starting from the noise-filtered spectral reflectivity (or spectral power density), the primary node contains the complete Doppler spectrum between $-v_{\mathrm{Nyq}}$ and $+v_{\mathrm{Nyq}}$. An example is shown in Fig. 1 (a) with the respective boundaries and moments in Tab. 1.

20 In a first step all noise-floor-separated peaks are added as child nodes with their boundaries v_{left} and v_{right} (in the example here -3.3 and $1.3\,\mathrm{m\,s^{-1}}$). Each node is then searched for relative minima in spectral reflectivity. If a node contains internal minima and hence subpeaks, it needs to be splitted into child nodes. All found minima are sorted by the spectral reflectivity from lowest to highest. Starting with the lowest minimum at v_{add} the node containing this minimum is split into two child nodes. When boundaries of the parent node are $[v_{\mathrm{left}}, v_{\mathrm{right}}]$, the left child node is $[v_{\mathrm{left}}, v_{\mathrm{add}}]$ and the right child node is $[v_{\mathrm{add}}, v_{\mathrm{right}}]$. In the

25 example from Fig. 1 (a) the internal minimum with the lowest spectral reflectivity is at $-0.2\,\mathrm{m\,s^{-1}}$ with a spectral reflectivity of $-33.4\,\mathrm{dBZ}$. This reflectivity also defines the threshold, that separates the subpeaks. The splitting at local minima is repeated for all remaining minima, always splitting the leaf node (i.e. a node that does not have any childs) in which the minimum is located. A minimum is skipped, when the prominence of one of its subpeaks is less than $1\,\mathrm{dB}$, where prominence is the height of the peak above the threshold that is definded by the local minimum (dashed grey lines in Fig 1 (a); similar to Shupe et al.,

30 2004).

In the next step the moments of the Doppler spectrum (reflectivity, mean velocity, width, skewness) are calculated for each node within its boundaries $[v_{\mathrm{left}}, v_{\mathrm{right}}]$ (see Appendix A). Only the part of the Doppler spectrum above the threshold defined by the spectral reflectivity minimum that separated the peaks are used. The LDR for this node is calculated using the spectral

Atmospheric
Measurement
Techniques
Discussions
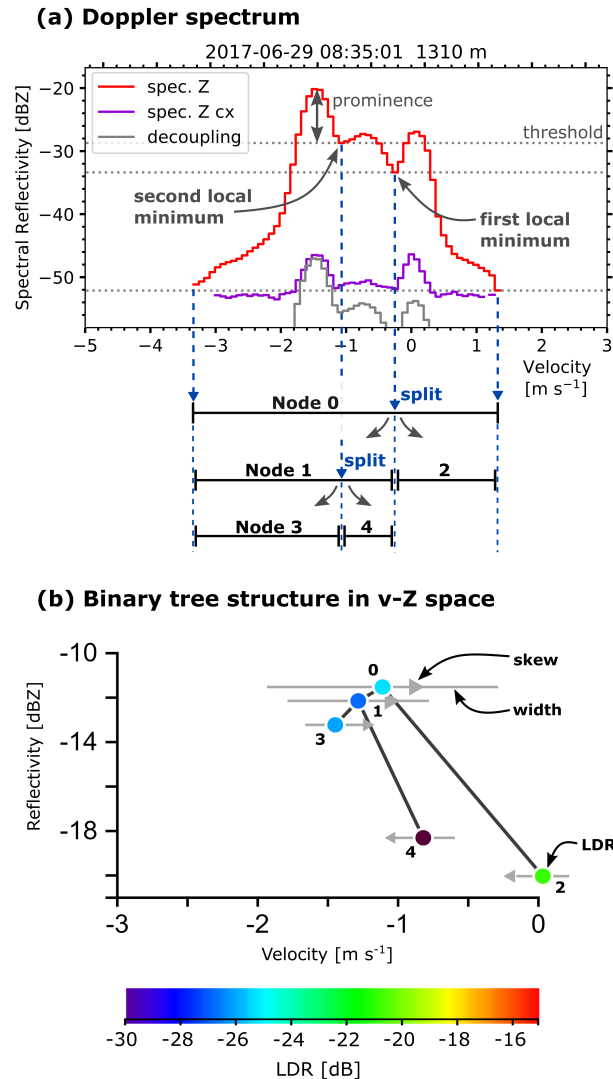
Figure 1. Example for generating the tree from a Doppler spectrum. An example spectrum at 29 June 2017 08:35:01 UTC at $1310\,\text{m}$ height is depicted in (a). The primary node (Node 0) is splitted into child-nodes at the indicated velocity bins (dashed blue) which contain a local minimum in spectral reflectivity. The threshold defined by the noise-floor and the internal minima is marked with dashed grey lines. (b) shows the resulting tree, where the location of a node in the v-Z space is based on its moments. Spectral width and skewness are shown by grey lines and triangles, respectively. The circle denoting the nodes position is color-coded in accordance to the nodes LDR.

reflectivity in the cross channel. Node 0 is similar to the moment estimation commonly used to analyze Doppler spectra (e.g. Carter et al., 1995; Clothiaux et al., 2000; Görsdorf et al., 2015). Its child nodes (1 and 2) are the subpeaks defined by the lowest relative minimum. The second lowest minimum then splits one of these nodes and gives nodes 3 and 4 (splitting node 1) or 5 and 6 (splitting node 2).

Atmospheric
Measurement
Techniques
Discussions

Table 1. Moments for each peak from the Doppler spectrum depicted in Fig. 1 with the index of the node according to the level-order tree traversal and the boundaries v_{left}, v_{right} are given in $\mathrm{m\,s^{-1}}$. Child-nodes are denoted by their level of indentation. The units are dBZ for Z and $\mathrm{m\,s^{-1}}$ for $\overline{v}$ and spectral width σ. The skewness γ is dimensionless, LDR is in dB. Both the threshold 'thres.' and the prominence 'prom.' are in dBZ.

Index	Boundaries $[v_{\text{left}}, v_{\text{right}}]$	Z	$\overline{v}$	σ	γ	LDR	thres.	prom.
0	`‘−` [-3.3, 1.3]	-11.57	-1.10	0.59	1.01	-25.3	-52.1	32.0
1	`+−` [-3.3, -0.2]	-12.19	-1.27	0.36	1.08	-26.9	-33.4	13.2
3	`|` `+−` [-3.3, -1.1]	-13.27	-1.44	0.15	0.27	-26.1	-28.7	8.5
4	`|` `‘−` [-1.1, -0.2]	-18.35	-0.81	0.16	-0.13	-32.2	-28.7	1.4
2	`‘−` [-0.2, 1.3]	-20.08	0.04	0.13	-0.31	-20.9	-33.4	6.2

The indices are based on level-order tree traversal and the index i of a node can be calculated by the following formulas:

$$i_{\text{left child}} = 2\,i_{\text{parent}} + 1 \tag{1}$$

$$i_{\text{right child}} = 2\,i_{\text{parent}} + 2 \tag{2}$$

$$i_{\text{parent}} = \left\lfloor \frac{i_{\text{child}} - 1}{2} \right\rfloor \tag{3}$$

5   Furthermore, the total number of subpeaks n_{subpeaks}, as estimated by established peak finding methods, can be calculated from the number of nodes n_{nodes}:

$$n_{\text{subpeaks}} = (n_{\text{nodes}} + 1)/2 \tag{4}$$

Each node is characterized by its reflectivity Z, vertical velocity v, spectral width, skewness, LDR and prominence. It is suitable to visualize the tree in the v-Z plane as a color-filled circle with the parent-child relationships depicted by a black line
10 (Fig. 1 b) and each circle is color-coded in accordance to its LDR. The width and skewness are shown by a horizontal grey line and a grey triangle with varying size, respectively. This representation combines all key parameters of a multipeak Doppler spectrum.

3.2   Grouping nodes into particle populations

The nodes representing similar particle populations in neighboring (time-height) bins can be connected to obtain a continuous
15 picture of the evolution of a particle population. First, a node is manually assigned to a particle population based on visual inspection and guided by the LDR value. These manually selected (anchor) nodes are spaced in steps of $50\,\mathrm{s}$ and $150\,\mathrm{m}$, making one anchor representative for a slice of 5 timestemps and 5 height bins or, in other words, for the 25 neighboring trees. For the time-height bins in between these anchor nodes, nodes with similar characteristics of the moments are automatically selected. Similarity is given, if a node is close to the anchor node in the v-Z space in minimal in terms of Euclidean distance
20 d and below a threshold $d < 0.9$. The parameters Z and v are normalized by factors of 5 and 0.3 respectively, to make both
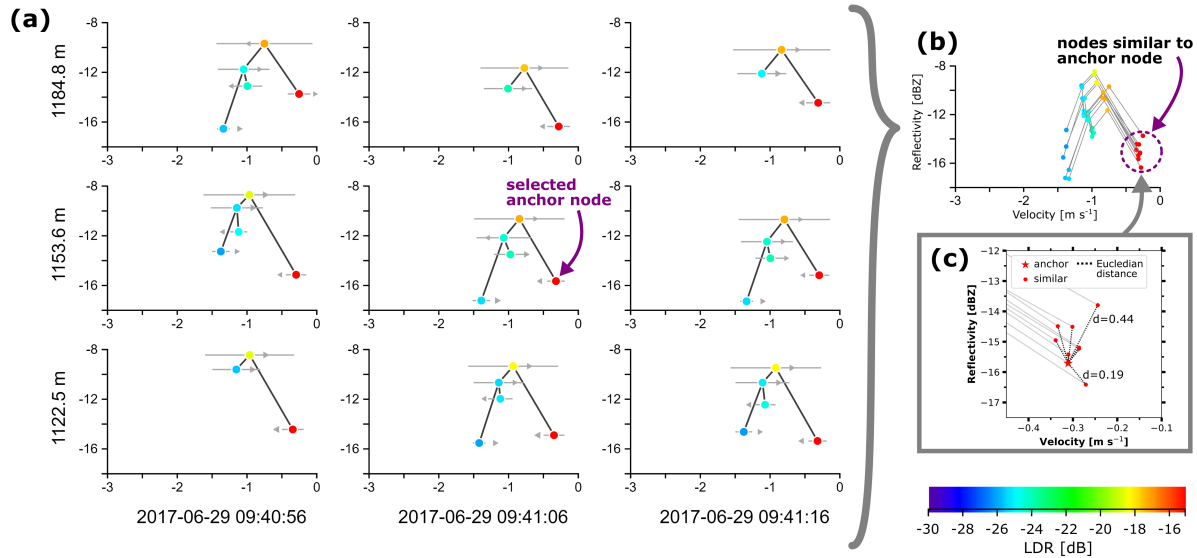
Figure 2. Illustration of the grouping algorithm for a single step. Single trees for a time-height slice are depicted in (a) with the selected anchor node marked by an arrow. The time-height cross section shown omits the outer trees of the 5×5 slice for clarity. The moments of each node are illustrated, as described in Fig. 1. In (b), the trees are combined into the same v-Z illustration with a circle denoting the nodes that are identified as similar by the Euclidean distance criterion. The Euclidean distance d is depicted in inset (c) for all nodes with index 2.

comparable for the grouping algorithm (Fig. 2). The sibling of these selected nodes is afterwards assigned to the second particle population.

4   Application: Separating two ice crystal habits in an Arctic cloud

On the 29 June 2017 R/V Polarstern was located a few nautical miles north of the island Kvitøya at $80.5°\text{N}, 31.5°\text{E}$. The
5   synoptic situation was controlled by a low over Fram strait with a secondary low that passed Polarstern on that day with the
surface wind veering from SE to NW and frequent light precipitation.

Between 08:30 and 09:45 UTC a cloud was continuously observed by Mira-35 from the surface up to $2.7\,\text{km}$ height with a
cloud top temperature of $-15°\text{C}$ (see Fig. 3). The thermodynamic structure of the cloud was probed by a RS92-SGP radiosonde,
that was launched from Polarstern at 10:50 UTC (Schmithüsen, 2017). The humidity profile shows saturation with respect to
10   liquid water throughout the whole cloud. Very light precipitation was observed at the surface by an optical disdrometer (Klepp
et al., 2018), peaking to $0.1\,\text{mm}\,\text{h}^{-1}$ at 08:50 UTC. The highest values of liquid water path ($\sim 50\,\text{g}\,\text{m}^{-2}$), obtained from the
microwave radiometer (Rose et al., 2005), were also observed during this time. Low reflectivity and vertical velocities close to
$0\,\text{m}\,\text{s}^{-1}$ with alternating up- and downdrafts suggest the presence of a turbulent liquid layer capping the cloud. Below $1.3\,\text{km}$
height, reflectivity and LDR of the single peak analysis show a sharp increase, giving hints to a change in microphysical
15   properties.

Atmospheric
Measurement
Techniques
Discussions
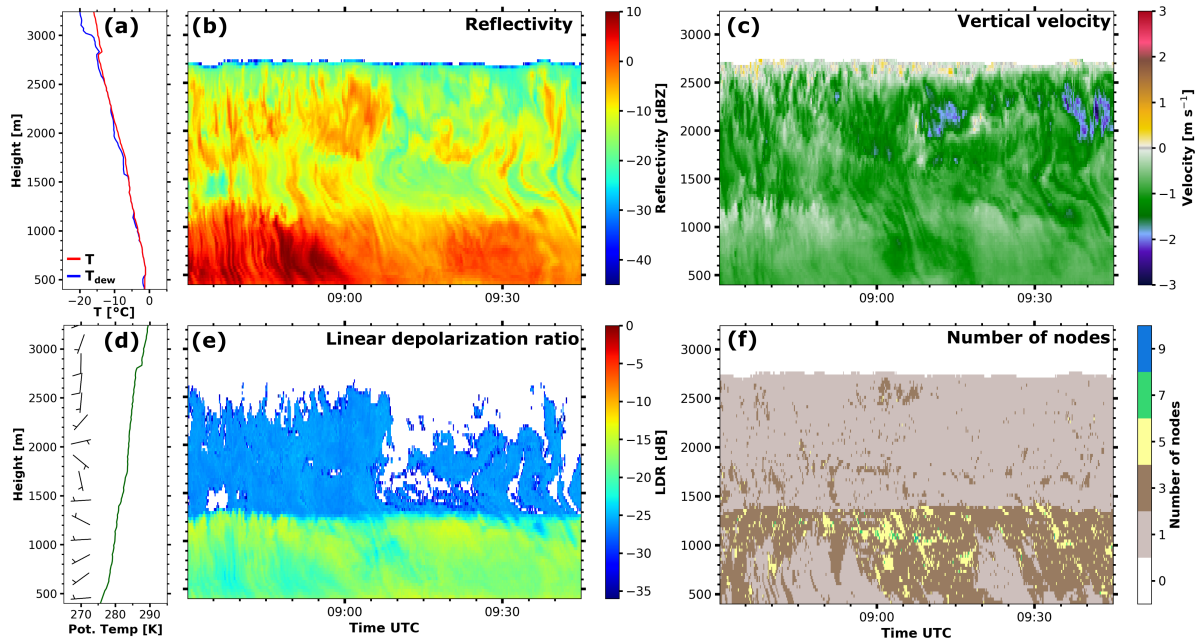
Figure 3. Radiosonde ascend at the 29 June 2017 10:50 UTC (a, d from Schmithüsen, 2017). Mira-35 reflectivity (b), mean velocity (c) and linear depolarization ratio (e) of the zeroth node (moments of the single peak analysis) at the 29 June 2017 from 08:30 to 09:45 UTC. Total number of nodes (f) for the same period.

Application of the multi-peak analysis introduced above reveals, that multi-peak spectra were quite frequent (Fig. 3 f). Nodes that are caused by liquid layers can not be depicted directly, but previous studies used the simple criterion of low reflectivity and vertical velocity close to $0\,\mathrm{m\,s^{-1}}$ to identify regions of a cloud, where the presence of liquid is likely (e.g. Shupe et al., 2001; Rambukkange et al., 2011; Yu et al., 2014; Kalesse et al., 2016). The thresholds used here are $Z < -20\,\mathrm{dBZ}$ and
5 $|v| < 0.3\,\mathrm{m\,s^{-1}}$. Obviously, this selection rule only applies, when the liquid peak is separated by a local minimum from the remainder of the Doppler spectrum. As shown in Fig 4, two continuous liquid layers at almost constant heights were observed during the whole case study. The top one at $2.7\,\mathrm{km}$ height topping the cloud is also visible in the single moments of the full spectrum. The second one at $1.3\,\mathrm{km}$ height, being hidden when only using the moments of the full spectrum. Furthermore, shorter periods of liquid water presence were detected, for example from 08:55 to 09:15 UTC at $1.0\,\mathrm{km}$ height. Together with
10 the lidar backscatter indicating a liquid cloud base at $750\,\mathrm{m}$ between 08:45 and 09:10 (attenuated at lower heights during the remaining time, not shown), this suggests the presence of an extended liquid layer not clearly visible in the Doppler spectra.

After grouping the nodes to particle populations (as explained in Section 3.2), the microphysical structure of this cloud becomes clearer. The faster-falling particle population (Fig. 5 left column) originating at the uppermost liquid layer at $2.7\,\mathrm{km}$ height has a rather variable reflectivity with background values of around $-20\,\mathrm{dBZ}$ and maxima in frequently occuring fall-
15 streaks of up to $0\,\mathrm{dBZ}$ reflectivity. The vertical velocity is quite variable as well. Below $2.5\,\mathrm{km}$ height, the generated ice

7
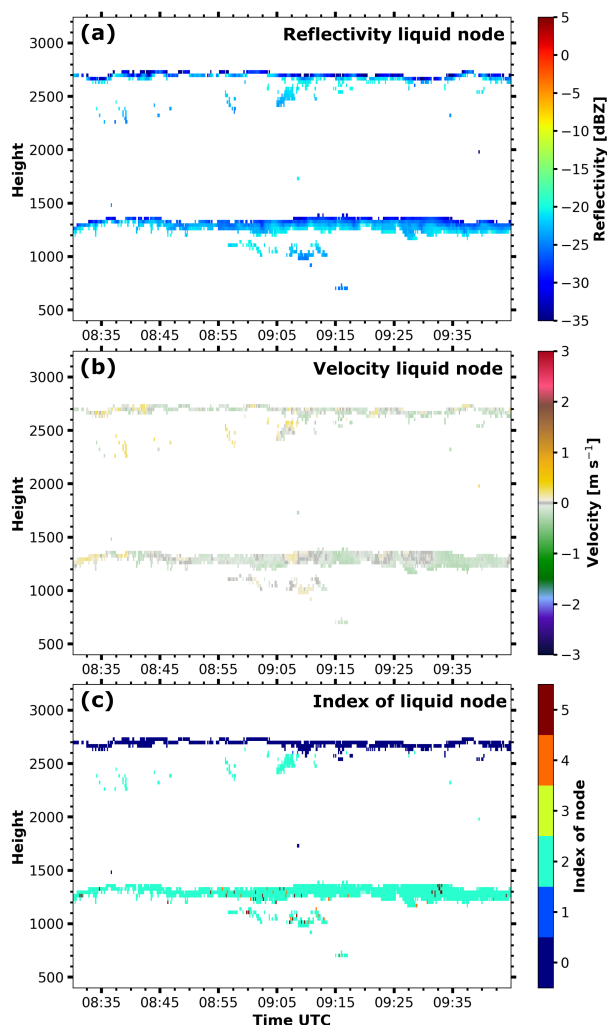
Figure 4. Reflectivity (a), mean velocity (b) and index of node (c) for nodes identified as supercooled liquid at the 29 June 2017 from 08:30 to 09:45 UTC.

particles descent with velocities of 0.5 and $2.0\,\mathrm{ms}^{-1}$. The low LDR of these particles (Fig. 5 e) is characteristic for prolate or plate-like particles (Myagkov et al., 2016), which is also consistent with particle habits formed at cloud top temperatures of around $-15°C$ (Bühl et al., 2016). Below the height of primary ice formation, several processes like depositional growth and and aggregation might contribute to particle growth.

5   Frequently, fallstreaks from the upper layer penetrate the second liquid layer at $1.3\,\mathrm{km}$ height. The lower-level liquid layer with a temperature of $-5°C$ also continuously forms ice (Fig. 5 right column). The vertical velocity is slower (-0.2 to $-0.7\,\mathrm{ms}^{-1}$) and more homogeneous than for the other particle population. The high LDR of $-14\,\mathrm{dB}$ at heights of 100 to $200\,\mathrm{m}$ below the top of the liquid layer can be attributed to columnar or needle-like ice crystals (Myagkov et al., 2016; Bühl et al.,

Atmospheric
Measurement
Techniques
Open Access
Discussions
EGU

2016). Hence, ice formation takes place between 1.1 and $1.3\,\mathrm{km}$ height which is also underpinned by the gradual increase of reflectivity and vertical velocity. Below $1.1\,\mathrm{km}$ height, the reflectivity is more variable, with maxima of $9\,\mathrm{dBZ}$ at 08:50 UTC and minima of $-11\,\mathrm{dBZ}$ at around 09:10 UTC. We cannot fully rule out that ice multiplication was triggered when the higher-level ice particles descended into the lower liquid layer. However, ice was formed from the lower liquid layer constantly over

5 time (Fig. 5 right column), even in periods where particles with very low reflectivity were potentially seeding from above, as it was the case for example between 09:10 und 09:30 UTC, which supports the interpretation, that at least a few ice crystals were caused by primary ice formation.

Looking into two individual fallstreaks, it is possible to track the evolution of the two particle populations. The selected fallstreaks are illustrated as black dashed curves in Fig. 5. In the frame of this study, the fallstreaks were selected manually

10 based on the criteria of following the signal maximum of the radar reflectivity of the faster falling particle population. It should be noted, that techniques for an automated classification of fallstreaks exist (Kalesse et al., 2016; Pfitzenmaier et al., 2017), which should be applied when longer time series are analysed. First hints for different microphysical processes become evident from tracking the properties of the individual nodes in the selected fallstreaks. The first one starts at 08:52 and $1.8\,\mathrm{km}$ height with a rather constant reflectivity of $-5\,\mathrm{dBZ}$ and a vertical velocity of around $-1.0\,\mathrm{ms}^{-1}$. The reflectivity is almost constant

15 down to $0.9\,\mathrm{km}$ height, after the fallstreak reaches the lower liquid layer. The LDR is unaffected by the liquid layer as well. Contrarily, the particle population generated within this liquid layer shows a strong increase in reflectivity from $-20\,\mathrm{dBZ}$ to $+6\,\mathrm{dBZ}$, while LDR decreases from $-14\,\mathrm{dB}$ to $-19\,\mathrm{dB}$. Below $0.8\,\mathrm{km}$ height, the faster falling mode is not longer visible as a separate peak (and accordingly the node disappears), because the slower falling population becomes dominant in the Doppler spectrum.

20 The second fallstreak, being less pronounced than the first one, begins at 09:06 and $1.5\,\mathrm{km}$ height with a reflectivity of $-10\,\mathrm{dBZ}$ and again a vertical velocity of around $-1.0\,\mathrm{ms}^{-1}$. After reaching the liquid layer at $1.3\,\mathrm{km}$ height, the reflectivity of this particle population increases to $-7\,\mathrm{dBZ}$ and also the velocity increases slightly. The LDR remains below $-25\,\mathrm{dB}$. The second particle population grows as well. From less than $-20\,\mathrm{dBZ}$ in the liquid layer to $-4\,\mathrm{dBZ}$ at $0.6\,\mathrm{km}$ with a final velocity of $-0.6\,\mathrm{ms}^{-1}$. During this growth, LDR remains at $-14\,\mathrm{dB}$, indicating no change in particle habit. Due to insufficient

25 polarimetric data, it is difficult to disentangle the contribution of different microphysical processes to particle growth. A more detailed investigation, using synergistic retrievals on top of the algorithm presented here, is required to pin-down the relevant processes further.

The ice water content (IWC) for each particle population can be retrieved from Z and the temperature (Hogan et al., 2006). This $Z-T$ retrieval was developed under the assumption of mono-modal peaks in the Doppler spectrum, but using the tree

30 structure it is possible to include the information from the Doppler spectrum into this retrieval rather easily. Fig. 6 shows the IWC for the full Doppler spectrum (a), hence assuming single-peaked spectra, and for the two separated particle populations (b, c). This opens the possibility to estimate the IWC for individual particle populations using established retrievals. As could also be seen in the discussion on the reflectivity of the particle populations above, the precipitation reaching the ground between 08:30 and 09:00 UTC could not be directly linked to cloud top ($2.7\,\mathrm{km}$), but was strongly modified by the internal liquid layer
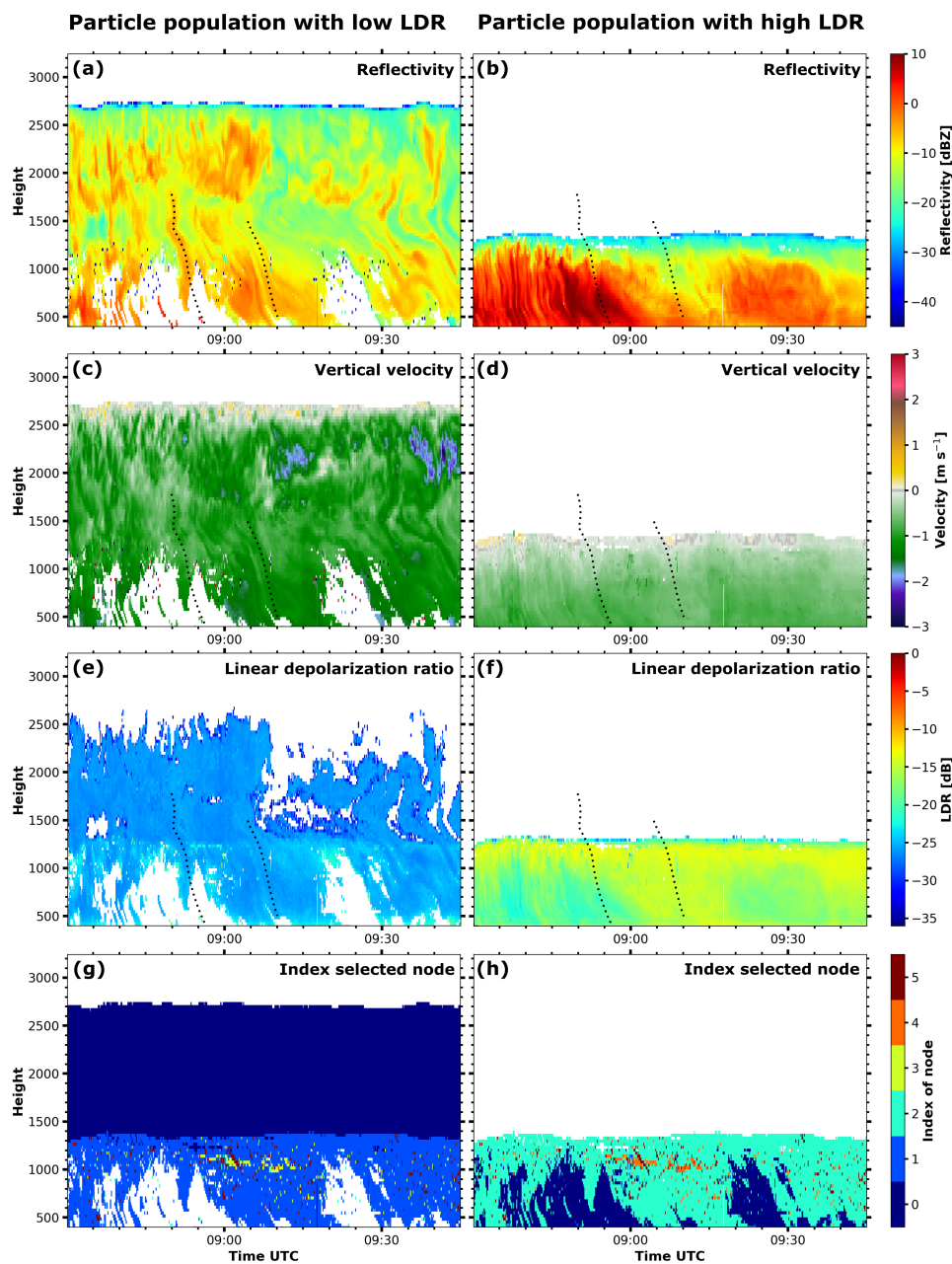
Figure 5. Reflectivity (a, b), mean velocity (c, d), linear depolarization ratio (LDR; e, f) and index of the selected node (g, h) of the two particle populations (left and right column) at the 29 June 2017 from 08:30 to 09:45 UTC. The dashed black lines locate the two fallstreaks described in the text. For regions marked in white no node could be assigned to the respective particle population.

at 1.3 km height. Following this approach, the proposed technique can also be used to extend the capabilities of established retrieval algorithms.
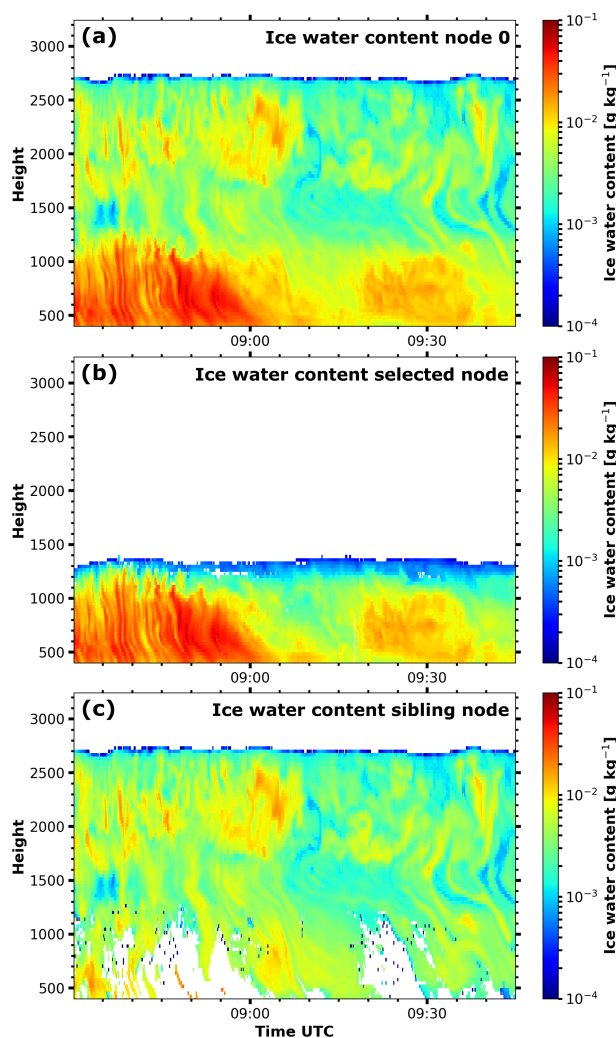
Figure 6. Retrieved ice water content from the full Doppler spectrum (a) and the two separated particle populations (b, c) at the 29 June 2017 from 08:30 to 09:45 UTC.

5 Discussion and Conclusions

We proposed a binary tree structure for individual peaks of a multi-peaked cloud radar Doppler spectrum. This data structure does not require prior assumptions on the arrangement or hierarchy of the peaks. The tree structure allows to select the level of complexity with which the Doppler spectrum is approximated, by the number of nodes taken into account. It also provides

backward compatibility, as the root node (i.e. node 0) holds the moments of the full Doppler spectrum with an implicit assumption of mono-modality. These moments are similar to standard Doppler spectra processing. Hence, a seamless transition from current single-peak techniques to multi-peak analysis is possible. This is an improvement compared, for example to microARSCL, where usually the primary peak (noise floor separated peak with the maximum of spectral reflectivity) is used

5   to represent the moments of the full spectrum.

In a second step we demonstrated a simple application this new structure by grouping nodes from neighboring Doppler spectra into particle populations based on their moments using the Euclidean distance in v-Z space. In this study, the anchor nodes had to be selected manually, but automatizing this selection should be also possible in a future step.

The technique was demonstrated by separating and sorting nodes into two particle populations in an Arctic mixed-phase

10   cloud. Looking at both particle populations individually can provide deeper insights into the prevalent physical processes. The upper liquid layer formed ice particles of, most likely, oblate shape as indicated by the LDR. While sedimenting, these particles grew further, either due to water vapor deposition or aggregation. When reaching a second liquid layer below, riming becomes available as a potential third growth process. Within this liquid layer a new ice particle population emerges. Using the tree representation of multi-peaked Doppler spectra, we were able to identify this second liquid layer and individually track

15   the evolution of the upper-level and the new ice particle population. Indications are given that new particles are formed: (1) the LDR signatures point toward prolate particles, which fits to the temperature in the second liquid layer and (2) ice is also produced in regions where ice fallstreaks from above are absent. Nevertheless, the characterization of the interactions between the two populations and further narrowing-down relevant growth processes would require a more-detailed investigation based on polarimetry or multi-wavelength radar and lidar synergy, which is beyond the scope of the current study. Furthermore, this

20   case study covers situations, where the assumption of the fastest falling subpeak was not the one with the highest reflectivity, as done by Oue et al. (2018), was violated.

In summary, we consider the peakTree approach a well-suited technique for enhancing the capabilities of cloud radar for the characterization of mixed-phase cloud processes. Tracing the evolution of polarimetric properties and velocity of distinct nodes will allow much more detailed studies of the ice growth and ice multiplication processes in future.

25   It is feasible to apply the algorithm also to Doppler spectra of other Doppler radars, as only very few parameters, namely the number of incoherent averages, the prominence, the noise threshold and - if a cross channel is available - the ICPR, need to be adjusted. Another extension would be to use other peak finding algorithms as an input for the tree generation. The only information required are at which Doppler bins the Doppler spectrum should be splitted. Furthermore, the tree structure can extend the capabilities of established classification algorithms and microphysical retrievals. Many of these methods are based

30   on single moment data and hence a mono-modal assumption. By applying the retrieval to each node individually, the strong assumption of mono-modality could be relaxed without major adjustments in the retrieval algorithm itself, as shown for the $Z - T$ ice water content retrieval.

Atmospheric
Measurement
Techniques
Discussions

Appendix A: Formulas for calculating the moments

5 The moments for each node in the Doppler spectrum are calculated following the formulas given by Maahn and Löhnert (2017) and Williams et al. (2018). $S(i)$ denotes the spectral reflectivity in the co channel at each bin i of the Doppler spectrum (not normalized by the width of the bin Δv) and the peak boundaries are $v_{\text{left}} = v(l)$, $v_{\text{right}} = v(r)$, where $v(i)$ maps the bin index to the velocity. $\overline{v}$ is the mean velocity, σ the spectral width and γ the skewness. For higher-order moments, tails of signal on side of the peak might cause a bias, when the other side is bound by an internal minimum (e.g. Fig. 1 (a) rightmost peak or

10 node 2, respectively.). To prevent this, only spectral reflectivity values $S(i)$ above the threshold that separates the subpeak from its neighbor are included for calculating moment other than Z.

$$Z = 10 \log_{10} \sum_{i=l}^{r} S(i) \tag{A1}$$

$$\overline{v} = \frac{\sum_{i=l}^{r} S(i)\, v(i)}{\sum_{i=l}^{r} S(i)} \tag{A2}$$

$$\sigma^2 = \frac{\sum_{i=l}^{r} S(i)\, [v(i) - \overline{v}]^2}{\sum_{i=l}^{r} S(i)} \tag{A3}$$

$$\gamma = \frac{\sum_{i=l}^{r} S(i)\, [v(i) - \overline{v}]^3}{\sigma^3 \sum_{i=l}^{r} S(i)} \tag{A4}$$

The LDR is calculated by using the spectral reflectivity in the cross channel $S_{cx}(i)$:

$$\text{LDR} = 10 \log_{10} \frac{\sum_{i=l}^{r} S_{cx}(i)}{\sum_{i=l}^{r} S(i)} \tag{A5}$$

Atmospheric
Measurement
Techniques
Open Access
Discussions
EGU

Atmospheric
Measurement
Techniques
Open Access
Discussions
EGU

References

Baumgardner, D., Abel, S. J., Axisa, D., Cotton, R., Crosier, J., Field, P., Gurganus, C., Heymsfield, A., Korolev, A., Krämer, M., Lawson, P., McFarquhar, G., Ulanowski, Z., and Um, J.: Cloud Ice Properties: In Situ Measurement Challenges, Meteorological Monographs, 58, 9.1–9.23, https://doi.org/10.1175/AMSMONOGRAPHS-D-16-0011.1, 2017.

5 Bühl, J., Alexander, S., Crewell, S., Heymsfield, A., Kalesse, H., Khain, A., Maahn, M., Van Tricht, K., and Wendisch, M.: Remote Sensing, Meteorological Monographs, 58, 10.1–10.21, https://doi.org/10.1175/AMSMONOGRAPHS-D-16-0015.1, 2017.

Bühl, J., Seifert, P., Myagkov, A., and Ansmann, A.: Measuring ice- and liquid-water properties in mixed-phase cloud layers at the Leipzig Cloudnet station, Atmospheric Chemistry and Physics, 16, 10 609–10 620, https://doi.org/10.5194/acp-16-10609-2016, 2016.

Carter, D. A., Gage, K. S., Ecklund, W. L., Angevine, W. M., Johnston, P. E., Riddle, A. C., Wilson, J., and Williams, C. R.:
10 Developments in UHF lower tropospheric wind profiling at NOAA's Aeronomy Laboratory, Radio Science, 30, 977–1001, https://doi.org/10.1029/95RS00649, 1995.

Clothiaux, E. E., Ackerman, T. P., Mace, G. G., Moran, K. P., Marchand, R. T., Miller, M. A., and Martner, B. E.: Objective Determination of Cloud Heights and Radar Reflectivities Using a Combination of Active Remote Sensors at the ARM CART Sites, Journal of Applied Meteorology, 39, 645–665, https://doi.org/10.1175/1520-0450(2000)039<0645:ODOCHA>2.0.CO;2, 2000.

15 Engelmann, R., Kanitz, T., Baars, H., Heese, B., Althausen, D., Skupin, A., Wandinger, U., Komppula, M., Stachlewska, I. S., Amiridis, V., Marinou, E., Mattis, I., Linné, H., and Ansmann, A.: The automated multiwavelength Raman polarization and water-vapor lidar Polly^{XT}: the neXT generation, Atmospheric Measurement Techniques, 9, 1767–1784, https://doi.org/10.5194/amt-9-1767-2016, https://www.atmos-meas-tech.net/9/1767/2016/, 2016.

Fan, J., Ghan, S., Ovchinnikov, M., Liu, X., Rasch, P. J., and Korolev, A.: Representation of Arctic mixed-phase clouds and the Wegener-
20 Bergeron-Findeisen process in climate models: Perspectives from a cloud-resolving study, Journal of Geophysical Research: Atmospheres, 116, https://doi.org/10.1029/2010JD015375, 2011.

Fukao, S. and Hamazu, K.: Radar for Meteorological and Atmospheric Observations, Springer, https://doi.org/10.1007/978-4-431-54334-3, 2014.

Garnier, R. and Taylor, J.: Discrete Mathematics: Proofs, Structures and Applications, Third Edition., CRC Press, Hoboken, 2009.

25 Griesche, H., Seifert, P., Baars, H., Engelmann, R., Radenz, M., Ansmann, A., and Macke, A.: Application of the shipborne remote-sensing supersite OCEANET for profiling of Arctic aerosols and clouds during Polarstern cruise PS106, 0, null, https://doi.org/-, in preparation.

Görsdorf, U., Lehmann, V., Bauer-Pfundstein, M., Peters, G., Vavriv, D., Vinogradov, V., and Volkov, V.: A 35-GHz Polarimetric Doppler Radar for Long-Term Observations of Cloud Parameters—Description of System and Data Processing, Journal of Atmospheric and Oceanic Technology, 32, 675–690, https://doi.org/10.1175/JTECH-D-14-00066.1, 2015.

30 Hogan, R. J., Mittermaier, M. P., and Illingworth, A. J.: The Retrieval of Ice Water Content from Radar Reflectivity Factor and Temperature and Its Use in Evaluating a Mesoscale Model, Journal of Applied Meteorology and Climatology, 45, 301–317, https://doi.org/10.1175/JAM2340.1, 2006.

Illingworth, A. J., Hogan, R. J., O'Connor, E. J., Bouniol, D., Delanoë, J., Pelon, J., Protat, A., Brooks, M. E., Gaussiat, N., Wilson, D. R., Donovan, D. P., Baltink, H. K., van Zadelhoff, G.-J., Eastment, J. D., Goddard, J. W. F., Wrench, C. L., Haeffelin, M., Krasnov, O. A.,
35 Russchenberg, H. W. J., Piriou, J.-M., Vinit, F., Seifert, A., Tompkins, A. M., and Willén, U.: Cloudnet: Continuous Evaluation of Cloud Profiles in Seven Operational Models Using Ground-Based Observations, Bulletin of the American Meteorological Society, 88, 883–898, https://doi.org/10.1175/BAMS-88-6-883, 2007.

Atmospheric
Measurement
Techniques
Discussions

Kalesse, H., Szyrmer, W., Kneifel, S., Kollias, P., and Luke, E.: Fingerprints of a riming event on cloud radar Doppler spectra: observations and modeling, Atmospheric Chemistry and Physics, 16, 2997–3012, https://doi.org/10.5194/acp-16-2997-2016, 2016.

Klepp, C., Michel, S., Protat, A., Burdanowitz, J., Albern, N., Kähnert, M., Dahl, A., Louf, V., Bakan, S., and Buehler, S. A.: Ocean-RAIN, a new in-situ shipboard global ocean surface-reference dataset of all water cycle components, Scientific Data, 5, 180 122,

5   https://doi.org/10.1038/sdata.2018.122, 2018.

Kollias, P., Clothiaux, E. E., Miller, M. A., Albrecht, B. A., Stephens, G. L., and Ackerman, T. P.: Millimeter-Wavelength Radars: New Frontier in Atmospheric Cloud and Precipitation Research, Bulletin of the American Meteorological Society, 88, 1608–1624, https://doi.org/10.1175/BAMS-88-10-1608, 2007a.

Kollias, P., Miller, M. A., Luke, E. P., Johnson, K. L., Clothiaux, E. E., Moran, K. P., Widener, K. B., and Albrecht, B. A.: The Atmospheric

10   Radiation Measurement Program Cloud Profiling Radars: Second-Generation Sampling Strategies, Processing, and Cloud Data Products, Journal of Atmospheric and Oceanic Technology, 24, 1199–1214, https://doi.org/10.1175/JTECH2033.1, 2007b.

Kollias, P., Clothiaux, E. E., Ackerman, T. P., Albrecht, B. A., Widener, K. B., Moran, K. P., Luke, E. P., Johnson, K. L., Bharadwaj, N., Mead, J. B., Miller, M. A., Verlinde, J., Marchand, R. T., and Mace, G. G.: Development and Applications of ARM Millimeter-Wavelength Cloud Radars, Meteorological Monographs, 57, 17.1–17.19, https://doi.org/10.1175/AMSMONOGRAPHS-D-15-0037.1, 2016.

15   Korolev, A., McFarquhar, G., Field, P. R., Franklin, C., Lawson, P., Wang, Z., Williams, E., Abel, S. J., Axisa, D., Borrmann, S., Crosier, J., Fugal, J., Krämer, M., Lohmann, U., Schlenczek, O., Schnaiter, M., and Wendisch, M.: Mixed-Phase Clouds: Progress and Challenges, Meteorological Monographs, 58, 5.1–5.50, https://doi.org/10.1175/AMSMONOGRAPHS-D-17-0001.1, 2017.

Luke, E. P. and Kollias, P.: Separating Cloud and Drizzle Radar Moments during Precipitation Onset Using Doppler Spectra, Journal of Atmospheric and Oceanic Technology, 30, 1656–1671, https://doi.org/10.1175/JTECH-D-11-00195.1, 2013.

20   Luke, E. P., Kollias, P., Johnson, K. L., and Clothiaux, E. E.: A Technique for the Automatic Detection of Insect Clutter in Cloud Radar Returns, Journal of Atmospheric and Oceanic Technology, 25, 1498–1513, https://doi.org/10.1175/2007JTECHA953.1, 2008.

Luke, E. P., Kollias, P., and Shupe, M. D.: Detection of supercooled liquid in mixed-phase clouds using radar Doppler spectra, Journal of Geophysical Research, 115, https://doi.org/10.1029/2009JD012884, 2010.

Maahn, M. and Löhnert, U.: Potential of Higher-Order Moments and Slopes of the Radar Doppler Spectrum for Retrieving Microphysical and

25   Kinematic Properties of Arctic Ice Clouds, Journal of Applied Meteorology and Climatology, 56, 263–282, https://doi.org/10.1175/JAMC-D-16-0020.1, 2017.

Matrosov, S. Y. and Kropfli, R. A.: Cirrus Cloud Studies with Elliptically Polarized Ka-band Radar Signals: A Suggested Approach, Journal of Atmospheric and Oceanic Technology, 10, 684–692, https://doi.org/10.1175/1520-0426(1993)010<0684:CCSWEP>2.0.CO;2, 1993.

Myagkov, A., Seifert, P., Wandinger, U., Bauer-Pfundstein, M., and Matrosov, S. Y.: Effects of Antenna Patterns on Cloud Radar Polarimetric

30   Measurements, Journal of Atmospheric and Oceanic Technology, 32, 1813–1828, https://doi.org/10.1175/JTECH-D-15-0045.1, 2015.

Myagkov, A., Seifert, P., Wandinger, U., Bühl, J., and Engelmann, R.: Relationship between temperature and apparent shape of pristine ice crystals derived from polarimetric cloud radar observations during the ACCEPT campaign, Atmospheric Measurement Techniques, 9, 3739–3754, https://doi.org/10.5194/amt-9-3739-2016, 2016.

Oue, M., Kollias, P., Ryzhkov, A., and Luke, E. P.: Toward Exploring the Synergy Between Cloud Radar Polarimetry and Doppler Spec-

35   tral Analysis in Deep Cold Precipitating Systems in the Arctic, Journal of Geophysical Research: Atmospheres, 123, 2797–2815, https://doi.org/10.1002/2017JD027717, 2018.

Pfitzenmaier, L., Dufournet, Y., Unal, C. M. H., and Russchenberg, H. W. J.: Retrieving Fall Streaks within Cloud Systems Using Doppler Radar, Journal of Atmospheric and Oceanic Technology, 34, 905–920, https://doi.org/10.1175/JTECH-D-16-0117.1, 2017.

Radenz, M., Bühl, J., and Seifert, P.: peakTree version of Feb2019, https://doi.org/10.5281/zenodo.2577387, 2019.

Rambukkange, M. P., Verlinde, J., Eloranta, E. W., Flynn, C. J., and Clothiaux, E. E.: Using Doppler Spectra to Separate Hydrometeor Populations and Analyze Ice Precipitation in Multilayered Mixed-Phase Clouds, IEEE Geoscience and Remote Sensing Letters, 8, 108–112, https://doi.org/10.1109/LGRS.2010.2052781, 2011.

5 Rose, T., Crewell, S., Löhnert, U., and Simmer, C.: A network suitable microwave radiometer for operational monitoring of the cloudy atmosphere, Atmospheric Research, 75, 183–200, 2005.

Schmithüsen, H.: Upper air soundings during POLARSTERN cruise PS106.2 (ARK-XXXI/1.2), https://doi.org/10.1594/PANGAEA.882843, 2017.

Shupe, M. D., Uttal, T., Matrosov, S. Y., and Frisch, A. S.: Cloud water contents and hydrometeor sizes during the FIRE Arctic Clouds
10   Experiment, Journal of Geophysical Research: Atmospheres, 106, 15 015–15 028, https://doi.org/10.1029/2000JD900476, 2001.

Shupe, M. D., Kollias, P., Matrosov, S. Y., and Schneider, T. L.: Deriving Mixed-Phase Cloud Properties from Doppler Radar Spectra, Journal of Atmospheric and Oceanic Technology, 21, 660–670, https://doi.org/10.1175/1520-0426(2004)021<0660:DMCPFD>2.0.CO;2, 2004.

Shupe, M. D., Comstock, J. M., Turner, D. D., and Mace, G. G.: Cloud Property Retrievals in the ARM Program, Meteorological Monographs, 57, 19.1–19.20, https://doi.org/10.1175/AMSMONOGRAPHS-D-15-0030.1, 2016.

15 Verlinde, J., Rambukkange, M. P., Clothiaux, E. E., McFarquhar, G. M., and Eloranta, E. W.: Arctic multilayered, mixed-phase cloud processes revealed in millimeter-wave cloud radar Doppler spectra, Journal of Geophysical Research: Atmospheres, 118, 199–213, https://doi.org/10.1002/2013JD020183, 2013.

Wakasugi, K., Mizutano, M., Matsuo, M., Fukao, S., and Kato, S.: A direct method of deriving drop size distribution and vertical air velocities from VHF Doppler radar spectra, Journal of Atmospheric and Oceanic Technology, 3, 623–629, https://doi.org/10.1175/1520-
20   0426(1986)003<0623:ADMFDD>2.0.CO;2, 1986.

Wang, Z. and Sassen, K.: Cirrus Cloud Microphysical Property Retrieval Using Lidar and Radar Measurements. Part I: Algorithm Description and Comparison with In Situ Data, Journal of Applied Meteorology, 41, 218–229, https://doi.org/10.1175/1520-0450(2002)041<0218:CCMPRU>2.0.CO;2, 2002.

Wang, Z., Sassen, K., Whiteman, D. N., and Demoz, B. B.: Studying Altocumulus with Ice Virga Using Ground-Based Active and Passive
25   Remote Sensors, Journal of Applied Meteorology, 43, 449–460, https://doi.org/10.1175/1520-0450(2004)043<0449:SAWIVU>2.0.CO;2, 2004.

Wendisch, M., Macke, A., Ehrlich, A., Lüpkes, C., Mech, M., Chechin, D., Dethloff, K., Barientos, C., Bozem, H., Brückner, M., Clemen, H.-C., Crewell, S., Donth, T., Dupuy, R., Ebell, K., Egerer, U., Engelmann, R., Engler, C., Eppers, O., Gehrmann, M., Gong, X., Gottschalk, M., Gourbeyre, C., Griesche, H., Hartmann, J., Hartmann, M., Heinold, B., Herber, A., Herrmann, H., Heygster, G., Hoor, P., Jafariser-
30   ajehlou, S., Jäkel, E., Järvinen, E., Jourdan, O., Kästner, U., Kecorius, S., Knudsen, E. M., Köllner, F., Kretzschmar, J., Lelli, L., Leroy, D., Maturilli, M., Mei, L., Mertes, S., Mioche, G., Neuber, R., Nicolaus, M., Nomokonova, T., Notholt, J., Palm, M., van Pinxteren, M., Quaas, J., Richter, P., Ruiz-Donoso, E., Schäfer, M., Schmieder, K., Schnaiter, M., Schneider, J., Schwarzenböck, A., Seifert, P., Shupe, M. D., Siebert, H., Spreen, G., Stapf, J., Stratmann, F., Vogl, T., Welti, A., Wex, H., Wiedensohler, A., Zanatta, M., and Zeppenfeld, S.: The Arctic Cloud Puzzle: Using ACLOUD/PASCAL Multi-Platform Observations to Unravel the Role of Clouds and Aerosol Particles in
35   Arctic Amplification, Bulletin of the American Meteorological Society, 0, null, https://doi.org/10.1175/BAMS-D-18-0072.1, in press.

Williams, C. R., Maahn, M., Hardin, J. C., and de Boer, G.: Clutter mitigation, multiple peaks, and high-order spectral moments in 35 GHz vertically pointing radar velocity spectra, Atmospheric Measurement Techniques, 11, 4963–4980, https://doi.org/10.5194/amt-11-4963-2018, 2018.

Yu, G., Verlinde, J., Clothiaux, E. E., and Chen, Y.-S.: Mixed-phase cloud phase partitioning using millimeter wavelength cloud radar Doppler velocity spectra, Journal of Geophysical Research: Atmospheres, 119, 7556–7576, https://doi.org/10.1002/2013JD021182, 2014.

Zhao, C., Xie, S., Klein, S. A., Protat, A., Shupe, M. D., McFarlane, S. A., Comstock, J. M., Delanoë, J., Deng, M., Dunn, M., Hogan, R. J., Huang, D., Jensen, M. P., Mace, G. G., McCoy, R., O'Connor, E. J., Turner, D. D., and Wang, Z.: Toward understanding of differences in current cloud retrievals of ARM ground-based measurements, Journal of Geophysical Research: Atmospheres, 117, https://doi.org/10.1029/2011JD016792, 2012.

5